



## Closing an open system: Pore pressure changes in permeable edifice rock at high strain rates



Michael J. Heap<sup>a,\*</sup>, Fabian B. Wadsworth<sup>b</sup>

<sup>a</sup> Géophysique Expérimentale, Institut de Physique de Globe de Strasbourg (UMR 7516 CNRS, Université de Strasbourg/EOST), 5 rue René Descartes, 67084 Strasbourg Cedex, France

<sup>b</sup> Earth and Environmental Sciences, Ludwig-Maximilians-Universität, Theresienstr. 41/III, 80333 München, Germany

### ARTICLE INFO

#### Article history:

Received 30 May 2015

Received in revised form 15 January 2016

Accepted 12 February 2016

Available online 24 February 2016

#### Keywords:

Pore pressure

Strain rate

Andesite

Drained

Undrained

Outgassing

### ABSTRACT

A permeable or open system will react as a closed system if the rocks implicated are deformed on a timescale that precludes fluid movement. Closed system (“undrained”) deformation therefore leads to a failure mode dependent change in pore pressure: microcracking (dilatant behaviour) and cataclastic pore collapse (compactant behaviour) will decrease and increase pore pressure, respectively. In the dilatant regime (i.e., in the shallow edifice, <1 km depth), a decrease in pore pressure will serve to strengthen rock—a process termed dilatancy hardening. However, it is shown here, using undrained triaxial deformation experiments, that the high initial porosity and microcrack density of typical edifice-forming andesites prevent dilatancy hardening. This allows the rock proximal to the magma-filled conduit in the shallow edifice to remain weak during periods of unrest when high magma strain rates could be transferred to the adjacent country rock. Although the propensity for fracturing will likely reduce the structural integrity of the edifice, fracturing of the shallow edifice may improve the outgassing efficiency of the nearby magma-filled conduit. The increase in pore pressure during undrained deformation in the compactant regime (i.e., in the deep edifice, >1 km depth) could lead to pore pressure embrittlement and fracturing. Indeed, the experiments of this study show that the pore pressure increases during progressive compaction in a closed system. However, the pore pressure is prevented from reaching the critical value required to promote a dilatant response (i.e., fracturing) for two reasons. First, the rate of compaction (i.e., porosity decrease) slows as the sample is deformed at a constant strain rate, a consequence of the decay in effective pressure. Second, the emergence of microcracking as the rock approaches the compactant–dilatant transition acts as a negative feedback and prevents the rock from transiting into the dilatant field. At this point, local porosity increases due to dilatant microcracking and local porosity decreases due to cataclastic pore collapse are balanced and the rock deforms without further changes to porosity or pore pressure. This will prevent potentially destabilising brittle failure deeper in the edifice during the high strain rates that may accompany unrest and, although it precludes the formation of efficient outgassing pathways in the form of fractures, undrained deformation in the compactant regime will prevent a reduction in porosity and permeability and may therefore facilitate lateral outgassing of the conduit into the country rock. We assess the conditions (strain rate and permeability) required for drained or undrained deformation by defining a dimensionless Darcy number. Closed system or undrained deformation is likely commonplace within a volcano (strain rates in the rock adjacent to an active volcanic system can be high and textural heterogeneities can serve as barriers to fluid flow) and therefore forms an important component for a complete understanding of the mechanical response of an edifice to the stress perturbations accompanying unrest.

© 2016 Elsevier B.V. All rights reserved.

### 1. Introduction

The rocks forming a volcanic edifice are subject to the stress perturbations that accompany volcanic unrest (e.g., Roman et al., 2004; Gerst and Savage, 2004). If the deformation of the edifice rock occurs on a timescale that precludes fluid movement—a function of the deformation rate and the permeability of the rock—the pore pressure inside edifice-forming rock will either increase or decrease in response to an imposed

stress. Deformation in the dilatant regime (the prevalent failure mode anticipated in the shallow edifice, <1 km; Heap et al., 2015a) will result in an increase in porosity (dilation; e.g., Brace et al., 1966; Read et al., 1995) and therefore, in the absence of fluid movement, a decrease in pore pressure. By contrast, compactant deformation (the prevalent failure mode anticipated in the deep edifice, >1 km; Heap et al., 2015a) will result in a decrease in porosity (compaction; e.g., Wong and Baud, 2012) and therefore an increase in pore pressure is expected in the absence of fluid migration.

For volcanic rock, the failure mode (dilatant or compactant) depends on the physical attributes of the rock (porosity and pore diameter,

\* Corresponding author.

E-mail address: [heap@unistra.fr](mailto:heap@unistra.fr) (M.J. Heap).

amongst others) and the prevalent pressure conditions, i.e. the effective pressure ( $P_{\text{eff}} = P_c - P_p$ , where the effective pressure  $P_{\text{eff}}$  is assumed to be equal to the confining pressure  $P_c$  minus the pore fluid pressure  $P_p$ ) (e.g., Heap et al., 2015a). In a scenario where the pore pressure can remain constant during deformation, high porosity volcanic rock ( $>0.1$ – $0.15$ ) will be dilatant in the shallow edifice ( $<1$  km depth; i.e., low effective pressures) and compactant at depth ( $>1$  km depth; i.e., high effective pressures) whilst low porosity volcanic rock ( $<0.1$ – $0.15$ ) will be dilatant at both low and high effective pressures (e.g., Kennedy et al., 2009; Zhu et al., 2011; Loaiza et al., 2012; Adelinet et al., 2013; Heap et al., 2015a, 2015b). In the dilatant field, deformation is manifested as localised axial splits or shear fractures (e.g., Loaiza et al., 2012; Adelinet et al., 2013; Heap et al., 2015a). Deformation in the compactive regime is characterised by either distributed cataclastic pore collapse (e.g., Zhu et al., 2011; Heap et al., 2015b) or the formation of localised bands of compacted pores (e.g., Loaiza et al., 2012; Adelinet et al., 2013; Heap et al., 2015a; Farquharson et al., 2016a).

In the dilatant field, an increase in the effective pressure (simplified here to be equivalent to an increase in depth in the edifice) increases the strength of rock (e.g., Paterson and Wong, 2005). Therefore, if the pore fluid pressure decreases due to dilatant deformation in a system that precludes fluid movement, the effective pressure will increase and the rock will strengthen. This phenomenon is called dilatancy hardening (e.g., Brace and Martin, 1968; Rice, 1975; Ismail and Murrell, 1976; Lockner and Stanchits, 2002; Paterson and Wong, 2005 and references therein). During deformation in the compactant field, in the absence of fluid movement, the increase in pore pressure as a result of compaction could reduce the effective pressure sufficiently to promote a dilatant response (i.e., fracturing)—a process termed pore pressure embrittlement (e.g., Farquharson et al., 2016a). In rock mechanics, the switch from a compactant to a dilatant failure mode is termed  $C^*$  (e.g., Schock et al., 1973; Baud et al., 2000, 2006; Heap et al., 2015a) and has previously been achieved through porosity loss and strain hardening in triaxial experiments in which the pore pressure is maintained at a constant value.

This study investigates: (1) dilatancy hardening in the dilatant regime and, (2) the potential for a switch in failure mode in the compactant regime in typical edifice-forming andesites (from Volcán de Colima, Mexico). To achieve these aims, triaxial experiments were performed in which water-saturated samples were deformed in a configuration in which water cannot enter or leave the sample (termed “undrained experiments” in studies of rock deformation; more information on undrained experiments is provided in the Materials and methods section). A scenario is envisaged in which saturated edifice host rocks experience a differential stress (e.g., the stress perturbations associated with magma ascent in the nearby magma-filled conduit) in a system that precludes drainage (deformation proceeds at a timescale that precludes fluid movement). The degree to which typical edifice rocks are water-saturated is therefore of particular interest to this study. The position of the water table beneath a stratovolcano can vary, and is a function of the rate of recharge, the heat input rate, and the hydraulic parameters of the system (Hurwitz et al., 2003). Although the water table at stratovolcanoes can be relatively deep (Hurwitz et al., 2003), perched water bodies, sandwiched between low-permeability layers, are also commonly observed or inferred at stratovolcanoes (e.g., Hurwitz et al., 2003; Finn et al., 2007).

In the scenario described above, dilatancy hardening could strengthen the edifice-forming rocks thereby increasing their resistance to fracture and promoting seismic quiescence (Scholz et al., 1973). A switch from a compactant to a dilatant failure mode in porous edifice rocks at depth could promote fracturing and provide new pathways for the lateral outgassing of the volcanic conduit in the adjacent country rocks (e.g., Jaupart, 1998; Collinson and Neuberg, 2012), or up through a fractured halo-zone that envelops the conduit (e.g., Rust et al., 2004; Lavallée et al., 2013; Gaunt et al., 2014; Plail et al., 2014; Young and Gottsmann, 2015). The ease with which exsolved gases can escape the

conduit can impact the style and intensity of an eruption. Generally speaking, efficient outgassing promotes effusive behaviour and inefficient outgassing promotes explosive behaviour (as discussed by many authors, e.g. Eichelberger et al., 1986; Woods and Koyaguchi, 1994). Deep fracturing, as a result of pore pressure embrittlement, could also reduce the structural stability of the edifice and increase the risk of flank collapse (e.g., Voight, 2000).

## 2. Materials and methods

For the purpose of this study, two edifice-forming andesites from Volcán de Colima (Mexico) were selected. Although the materials are sourced from Volcán de Colima, the concepts presented in this study will be applicable to many active and frequently-collapsing andesitic stratovolcanoes, such as Ruapehu (New Zealand), Soufrière Hills volcano (Montserrat), Merapi (Indonesia), Santa María (Guatemala), and Tungurahua (Ecuador). The first block, C8, was taken from the 1998–1999 block-and-ash flow in the San Antonio ravine and contains a connected porosity of about 0.165. The second, B5, is from an older lava of unknown age and contains a connected porosity of about 0.075. The locations of the collection sites are indicated in Heap et al. (2014a; 2015a). Both andesites have a porphyritic texture consisting of a glassy groundmass containing abundant microlites and pores (59–68 vol.%) and a (commonly microcracked) phenocryst cargo ( $<1.5$  mm in diameter) of plagioclase (13–25 vol.%), clinopyroxene (3–4 vol.%), and orthopyroxene (2–4 vol.%). The crystal fraction does

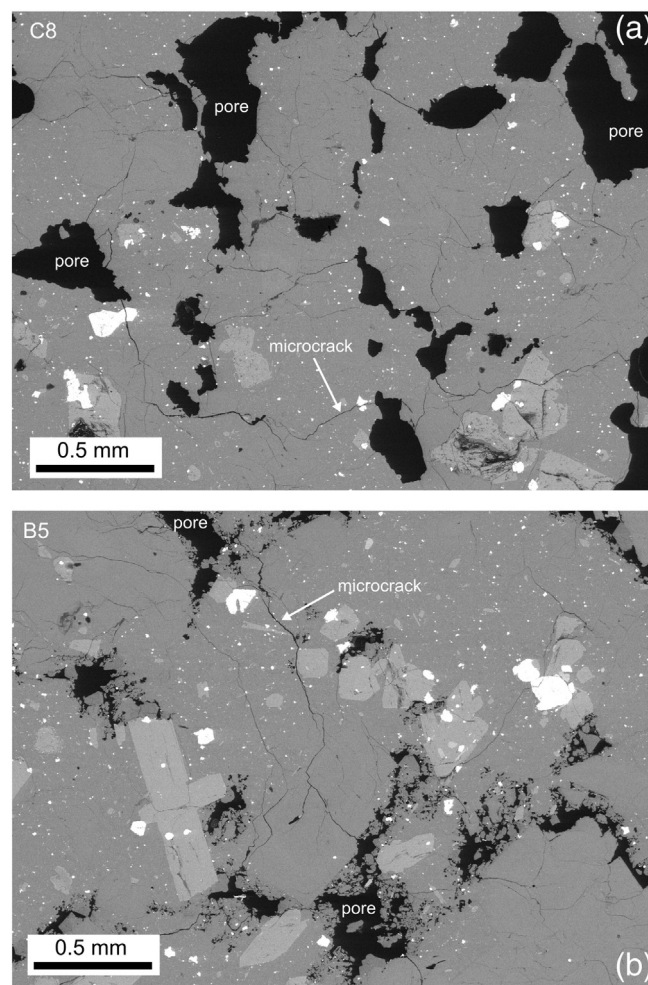


**Fig. 1.** The microstructure of the studied andesites from Volcán de Colima. (a) Back-scattered scanning electron microscope image of C8. (b) Back-scattered scanning electron microscope image of B5. The microstructural elements are highlighted on the pictures.

**Table 1**

Average physical properties of the two andesite blocks—C8 and B5—used in this study. Data from Heap et al. (2014a). Connected porosity and permeability were measured under confining pressures of 0.1 MPa (atmospheric) and 2 MPa, respectively.

Block	C8	B5
Connected porosity	0.165	0.075
Water permeability $k$ ( $\text{m}^2$ )	$5 \times 10^{-13}$	$4 \times 10^{-17}$
Microcrack surface area per $\text{mm}^3$ ( $\text{mm}^{-1}$ )	40.8	42.2
Pore number density ( $\text{mm}^{-2}$ )	3.27	6.13

not vary significantly between the two blocks. The andesites of this study contain a dual porosity of microcracks and pores (i.e. vesicles) (Fig. 1; Heap et al., 2014a). C8 and B5 are pervasively microcracked and contain high pore number densities and a wide pore size distribution (Table 1; Heap et al., 2014a). The permeability  $k$  of C8 and B5 (measured using distilled water and under a confining pressure of 2 MPa) is about  $5 \times 10^{-13}$  and  $4 \times 10^{-17} \text{ m}^2$ , respectively (Table 1; Heap et al., 2014a). We note that B5 displays evidence of high temperature alteration (Heap et al., 2015a). Cylindrical samples, cored to a diameter of 20 mm and precision-ground to a nominal length of 40 mm, were prepared from the two blocks. The connected water porosities of the samples were measured using the triple weight water-saturation (distilled water) method using Archimedes' principal (Guéguen and Palciauskas, 1994).

A first series of triaxial experiments ( $\sigma_1 > \sigma_2 = \sigma_3$ ) were performed on water-saturated samples of C8 and B5 at a confining pressure  $P_c$  of 20 MPa and an initial pore pressure  $P_p$  of 10 MPa. Under an effective pressure  $P_{\text{eff}}$  of 10 MPa, both C8 and B5 are within the dilatant regime (Heap et al., 2015a). For the purpose of this study we assume a simple effective pressure law where  $P_{\text{eff}} = P_c - \alpha P_p$  for which the poroelastic constant  $\alpha$  is 1. A recent study by Farquharson et al. (2016a) demonstrated that  $\alpha$  for porous andesite is extremely close to 1, validating our assumption. The samples were then deformed at a constant axial strain rate of  $10^{-5} \text{ s}^{-1}$  until macroscopic failure. During the experiments the pore fluid (distilled water) within the sample was isolated from the pore pressure intensifier, i.e. the experiments were undrained (the volume of pore fluid inside the rock is constant).

A second series of undrained triaxial experiments were performed on water-saturated samples of C8 at confining pressures of 40 and 60 MPa and an initial pore pressure of 10 MPa. Experiments have previously shown that, under these conditions, C8 is within the compactive regime (Heap et al., 2015a). A schematic representation of drained and undrained triaxial experiments (in the compactant regime) is provided as Fig. 2. Due to instances of compaction localisation (Loaiza et al., 2012; Adelinet et al., 2013; Heap et al., 2015a), and the observation that macroscopically “ductile” behaviour (defined as the capacity of a material to deform to a substantial strain without the tendency to localise the flow into faults; Rutter, 1986) can be driven by microcracking in the case of cataclastic flow, the classification of a “ductile” failure mode is simplified to “compactant” in this manuscript. The andesites deformed in the compactive regime were deformed at a constant axial strain rate of  $10^{-5} \text{ s}^{-1}$  until an axial strain of 6%. The undrained experiments of this study are compared with drained experiments (on the same materials and under the same pressure conditions) from Heap et al. (2015a) and Farquharson et al. (2016a).

During all of the experiments, an external load cell recorded axial load and the axial shortening (strain) of the samples was measured using an external linear variable differential transformer (LVDT), which monitored the movement of the axial piston relative to the static pressure vessel. The pore pressure during the tests was monitored using a pressure transducer; sample porosity change, however, could not be determined during the undrained experiments since its measurement relies on the pore pressure intensifier/volumometer. Acoustic emission (AE) energy (the root-mean-square of the received waveform) was monitored using a single piezoelectric crystal attached to the top piston (see Heap et al., 2014b for further details on the experimental setup). All

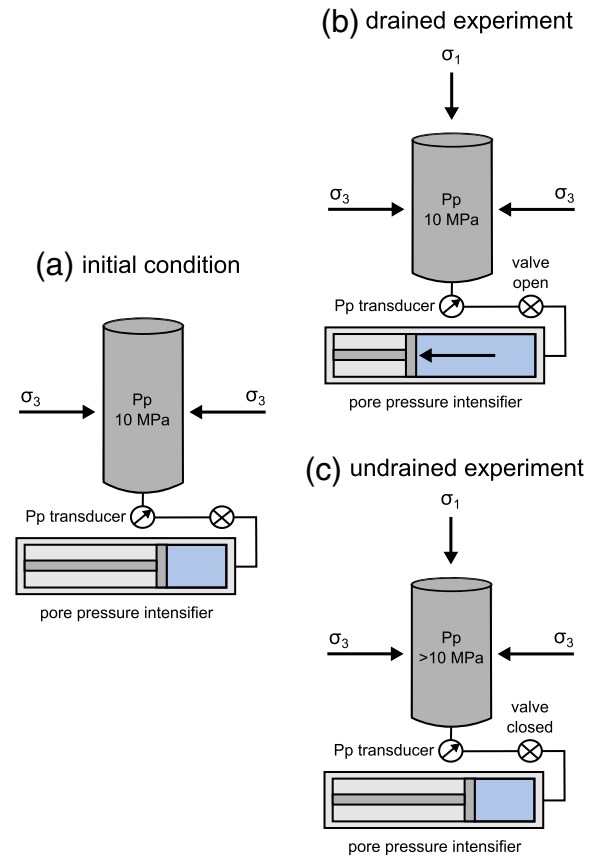


**Fig. 2.** Schematics highlighting the difference between a drained and an undrained experiment, shown here for experiments performed in the compactant (porosity reduction) regime. (a) The cylindrical sample before deformation: the confining pressure ( $\sigma_3$ ) and pore fluid pressure ( $P_p$ ) have been applied by means of a confining pressure intensifier (not shown) and a pore pressure intensifier. (b) In the drained experiment, as the sample compacts the pore pressure intensifier moves back (taking water from the sample) to maintain a constant pore pressure. (c) In the undrained experiment, the valve to the pore pressure intensifier is closed and so, as the sample compacts, the pore pressure within the sample rises.

of the experiments presented in this study were performed at room temperature. This is justified because, once deposited and cooled, these materials are unlikely to exceed the glass transition temperature of the amorphous groundmass glass phase ( $\sim 740 \text{ }^\circ\text{C}$  measured at  $\sim 10 \text{ }^\circ\text{C}/\text{min}$  heating rate from a known imposed cooling rate; Lavallée et al., 2012). We propose, therefore, that these experiments probe behaviours relevant to edifice deformation processes. In this study we adopt the convention that compressive stresses and strains are positive.

### 3. Results

#### 3.1. Dilatancy hardening in the dilatant regime?

The stress–strain curves, and the evolution of pore pressure and effective pressure as a function of strain, for the undrained samples of andesite deformed in the dilatant regime ( $P_c = 20 \text{ MPa}$ ;  $P_p = 10 \text{ MPa}$ ) are presented in Fig. 3, alongside data from drained experiments under the same pressure conditions (from Heap et al., 2015a and Farquharson et al., 2016a). In the dilatant regime, the stress is a non-linearly increasing function of strain, which is attributed to the closure of pre-existing microcracks, followed by a quasi-linear elastic portion (Fig. 3a and d). Following elastic deformation, the stress is a non-linearly decreasing function of strain prior to a peak stress, which is a result of the nucleation and growth of microcracks. Evidence for this is the onset and subsequent acceleration in AE activity coincident

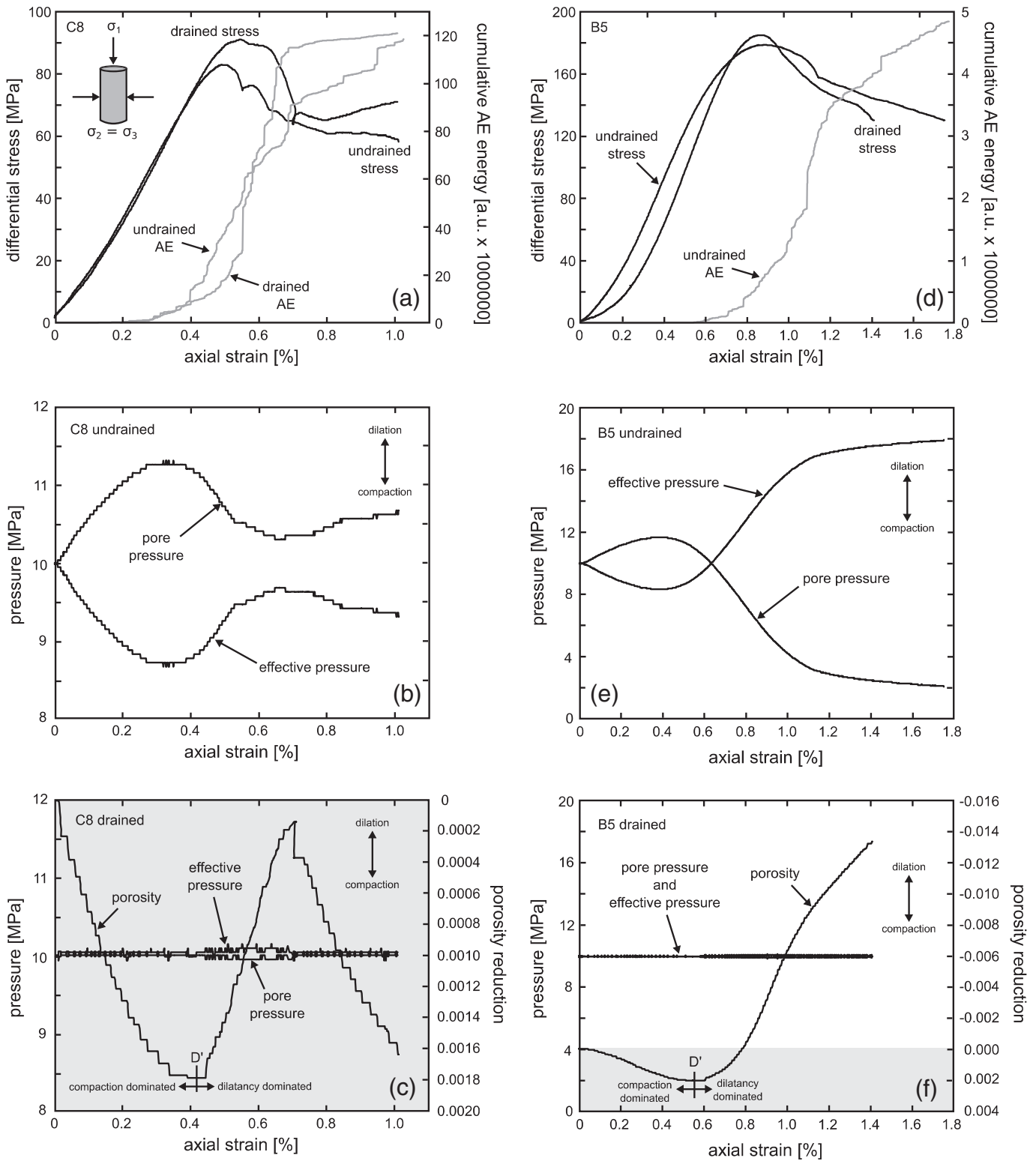


**Fig. 3.** The evolution of stress, AE output, pore pressure, effective pressure, and porosity with increasing axial strain during drained and undrained triaxial experiments in the dilatant regime ( $P_c = 20$  MPa and initial  $P_p = 10$  MPa). (a) Stress–strain curves for the drained and undrained experiments (black curves) on samples of C8, together with the output of AE energy (grey curves). (b) The evolution of pore pressure and effective pressure during the undrained deformation of the sample of C8 shown in panel (a). (c) The evolution of porosity, pore pressure, and effective pressure during the drained deformation of the sample of C8 shown in panel (a). The area of net compaction is highlighted in grey. (d) Stress–strain curves for the drained and undrained experiments (black curves) on samples of B5, together with the output of AE energy for the undrained experiment (grey curve). AE energy was not recorded for the drained experiment of Heap et al. (2015a). (e) The evolution of pore pressure and effective pressure during the undrained deformation of the sample of B5 shown in panel (d). (f) The evolution of porosity, pore pressure, and effective pressure during the drained deformation of the sample of B5 shown in panel (d). The area of net compaction and net dilation are highlighted in grey and white, respectively.

with the departure from quasi-linear elasticity. Following the peak stress the rock enters a strain-softening phase, preceded by a stress drop marking the strain at which macroscopic sample failure occurred (Fig. 3a and d). Finally, additional post-failure strain is accommodated by sliding on the resultant shear fracture at the residual frictional strength.

For the high porosity andesite (sample C8 with a porosity of 0.165) deformed under undrained conditions, the pore pressure first increased to 11.3 MPa. This is a consequence of the expulsion of water from closing pre-existing microcracks (Fig. 3b). The onset of AE activity (Fig. 3a) suggests that dilatant microcracking slowed the rate of pore pressure increase and, at a differential stress of about 50 MPa, the pore pressure began to decrease (Fig. 3a and b). The switch from pore pressure increase to pore pressure decrease is analogous to the switch from compaction- to dilatant-dominated behaviour in drained experiments (termed D'; Fig. 3c). The pore pressure was ~11 MPa at the peak stress (at an axial strain of ~0.5%), and reached a low of 10.4 MPa at an axial strain of ~0.7%. This minimum pore pressure occurred after the peak stress and the formation of a shear fracture. Subsequent sliding on the fault plane served to increase the pore pressure (Fig. 3b). The small changes in pore pressure were insufficient to severely impact the mechanical behaviour of the undrained sample, which was remarkably similar to that of the drained sample (Fig. 3a).

The pore pressure increase due to the closure of microcracks was similar for the low porosity andesite (sample B5 with a porosity of 0.075) during undrained deformation, reaching a high of 11.6 MPa (Fig. 3e). A higher differential stress (Fig. 3d) and a larger volume of dilatant microcracks are required for brittle failure in the low porosity samples compared with the high porosity samples. Evidence for this is found in the curves of porosity as a function of time for the drained experiments: the total porosity increase at failure is greater for the low porosity samples (Fig. 3f). For these reasons, the undrained deformation of low porosity rock should result in a larger decrease in pore pressure and therefore holds the greater potential for dilatancy hardening. Indeed, dilatant microcracking and shear fracture formation reduced the pore pressure to 2.9 MPa (at a strain of about 1.2%; Fig. 3e), although the pore pressure at the peak stress was 7.5 MPa. However, despite the reduction in pore pressure, the stress–strain curves for the undrained and drained experiments are essentially identical (Fig. 3d). Although, one should note that both undrained samples are measurably weaker (Fig. 3a and d; Table 2). Therefore, it can be concluded that, under the conditions studied here, dilatancy hardening did not occur in either andesite sample (porosity = 0.165 and 0.075).

### 3.2. Switch from a compactant to a dilatant failure mode?

The stress–strain curves, and the evolution of pore pressure and effective pressure as a function of strain, for the undrained samples of andesite deformed in the compactive regime ( $P_c = 40$  and 60 MPa;  $P_p = 10$  MPa) are presented in Fig. 4a and b, together with data from drained

experiments under the same pressure conditions (Fig. 4c and d; from Heap et al., 2015a and Farquharson et al., 2016a). The compactant stress–strain curves also show that the stress is initially an increasing function of strain; this is followed by a quasi-linear elastic deformation portion (Fig. 4a and c). The samples depart from poroelastic behaviour at a critical stress state termed the onset of shear-enhanced compaction or  $C^*$  (Wong et al., 1997). Subsequent deformation proceeds without significant strain softening and without a large stress drop, such that the deformation is entirely compactant (Fig. 4d). The stress–strain behaviour in this portion of the stress–strain curve is characterised by many small stress drops and, in some cases, strain hardening (e.g., the  $P_c = 50$  MPa curve in Fig. 4c). Such small stress drops during compactant deformation of porous volcanic rocks has been previously attributed to compactant strain localisation (Heap et al., 2015a).

For the undrained experiment at an initial effective pressure of 30 MPa, the pore pressure increased to 22 MPa (from a starting pressure of 10 MPa) at an axial strain of 6%, resulting in a decrease in effective pressure to 18 MPa (Fig. 4b). The pore pressure increased to 36 MPa at a starting effective pressure of 50 MPa, reducing the effective pressure to 24 MPa (Fig. 4b). The drained experiments show that there is a continuous reduction in porosity during deformation, as a result of cataclastic pore collapse (see also Heap et al., 2015a). This porosity reduction slows as axial strain increases (Fig. 4d). The observed slow reduction in porosity during the drained experiments suggests that we should expect a slow reduction in the rate of pore pressure increase during the undrained experiments. However, the rate of pore pressure accumulation with increasing strain in the undrained experiments slows considerably (Fig. 4b) and, for the experiment at an initial effective pressure of 30 MPa, the pore pressure (and therefore the effective pressure) appears to plateau at an axial strain of ~5.5%. The stress at the onset of shear-enhanced compaction is also reduced for samples deformed under undrained conditions (Table 2). Despite these differences, no significant changes are observed in the stress–strain curves between the drained (Fig. 4c) and undrained (Fig. 4a) experiments, although the drained experiment at an effective pressure of 50 MPa shows more much in the way of strain hardening behaviour compared with its undrained counterpart. An important point to note is that the undrained experiments did not switch to a dilatant mode of failure (Fig. 4a).

## 4. Discussion

### 4.1. Porous andesites do not exhibit dilatancy hardening during undrained deformation

Direct comparisons between drained and undrained triaxial experiments in the dilatant regime show that the porous andesites of this study do not experience dilatancy hardening during undrained deformation. This is an observation in stark contrast with similar experiments on low-porosity crustal rocks (e.g., Brace and Martin, 1968). In the case of low-porosity rocks (porosity = 0.01–0.03), the dilatancy-induced

**Table 2**  
Experimental summary of the 8 experiments presented in this study.

Block	Sample	Initial connected porosity	Confining pressure (MPa)	Pore pressure (MPa)	Effective pressure (MPa)	Strain rate ( $s^{-1}$ )	Peak differential stress (MPa)	$C^*$ (MPa)	P (MPa)	Notes
B5	7 <sup>a</sup>	0.074	20	10	10	$10^{-5}$	184.9	–	71.6	Drained
B5	13	0.076	20	10	10	$10^{-5}$	178.7	–	69.6	Undrained
C8	41	0.164	20	10	10	$10^{-5}$	83.0	–	37.7	Undrained
C8	13 <sup>b</sup>	0.160	20	10	10	$10^{-5}$	91.1	–	40.4	Drained
C8	38	0.165	40	10	30	$10^{-5}$	–	44.6	44.9	Undrained
C8	32 <sup>b</sup>	0.161	40	10	30	$10^{-5}$	–	48.4	46.1	Drained
C8	37	0.166	60	10	50	$10^{-5}$	–	45.3	65.1	Undrained
C8	4 <sup>a</sup>	0.164	60	10	50	$10^{-5}$	–	60.3	70.1	Drained

<sup>a</sup> Experiments taken from Heap et al. (2015a).

<sup>b</sup> Experiments taken from Farquharson et al. (2016a).

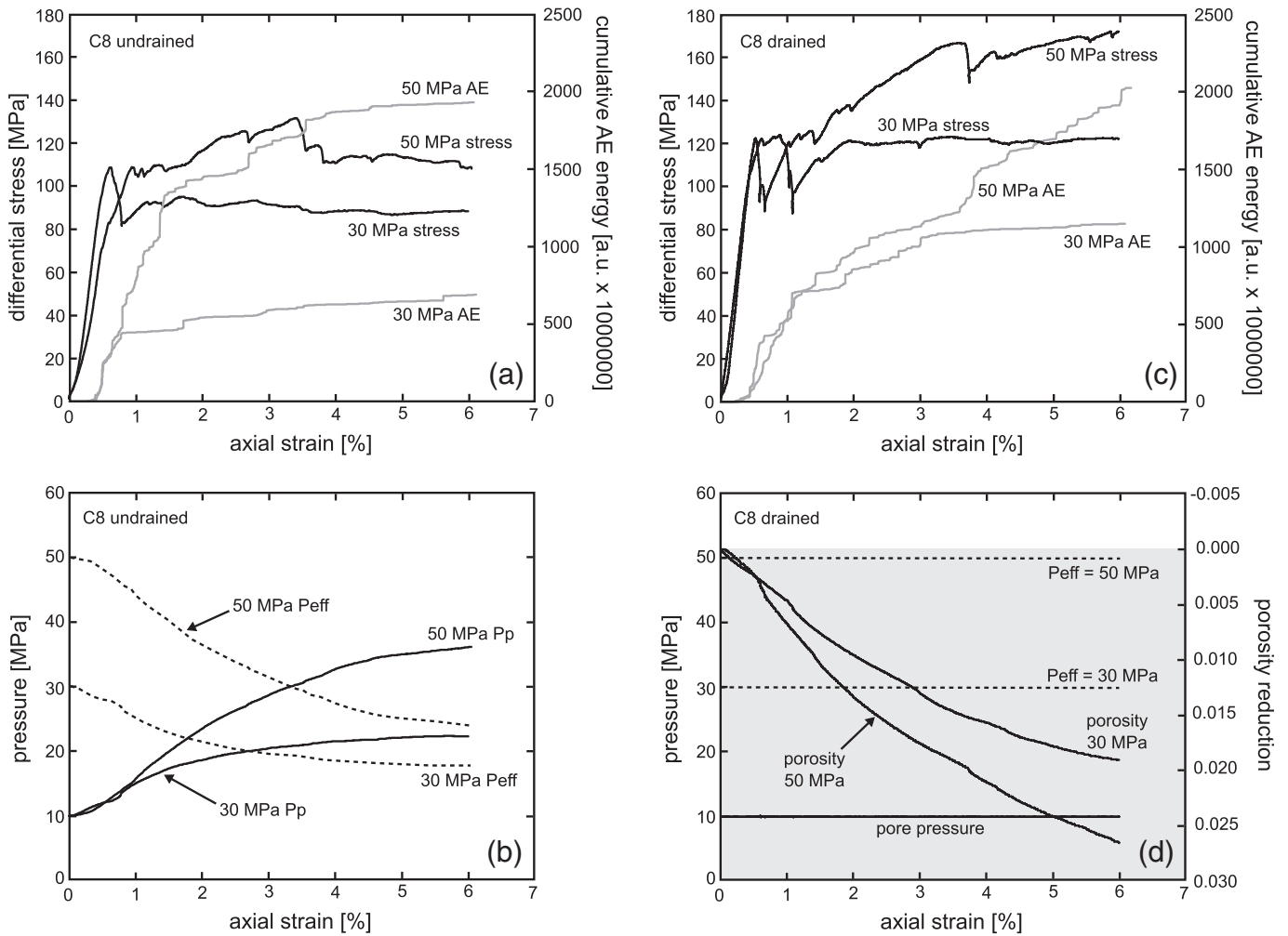


**Fig. 4.** The evolution of stress, AE output, pore pressure, effective pressure, and porosity with increasing axial strain during drained and undrained triaxial experiments in the compactant regime ( $P_c = 40$  and  $60$  MPa and initial  $P_p = 10$  MPa). (a) Stress–strain curves for the undrained experiments on samples of C8 (black curves), together with the output of AE energy (grey curves). The initial effective pressure is indicated next to each curve. (b) The evolution of pore pressure and effective pressure during the undrained deformation of the samples of C8 shown in panel (a). The initial effective pressure is indicated next to each curve. (c) Stress–strain curves for the drained experiments on samples of C8 (black curves), together with the output of AE energy (grey curves). The initial effective pressure is indicated next to each curve. (d) The evolution of porosity, pore pressure, and effective pressure ( $P_{eff}$ ) during the drained deformation of the samples of C8 shown in panel (c). The initial effective pressure is indicated next to each curve.

porosity resulting from the initiation and growth of microcracks can increase the porosity by a factor of 2 or 3 (Brace and Martin, 1968). It follows that this results in a substantial reduction in pore pressure such that dilatancy hardening can ensue. However, in the case of higher porosity rocks, such as those studied here, the additional porosity resulting from dilatational microcracking represents a much smaller percentage of the initial porosity, and therefore the reduction in pore pressure required to significantly harden the rock may be unreachable. In the case of the andesites studied here, an important factor controlling the absence of dilatancy hardening is their high initial microcrack density (Table 1). The high initial microcrack density of the andesites resulted in an initial decrease in porosity, and therefore pore pressure increase as favourably-orientated microcracks close in response to the differential stress (Fig. 3). In fact, the pore pressure only returned to the initial value of 10 MPa immediately prior to failure in B5 (at an axial strain of  $\sim 0.7\%$ ; Fig. 3). During undrained deformation of C8, the pore pressure never fell below the initial 10 MPa (Fig. 3b). Therefore, prior to the peak stress, the samples spent most or all of their time deforming at an effective pressure lower than that imposed at the start of the experiments. This not only explains the absence of dilatancy hardening, but may also explain the fact that the undrained samples are both measurably weaker than the drained samples (Fig. 3a and d; Table 2). We anticipate

that volcanic rocks containing the high microcrack densities typical of edifice-building materials will not harden through dilatancy, and may even fail at a lower differential stress if deformation occurs in the absence of fluid movement (i.e., undrained conditions).

#### 4.2. Porous andesites do not switch to a dilatant failure mode during undrained deformation

Undrained triaxial experiments on porous andesites in the compactive regime show that a switch to a dilatant mode of failure, as a result of the increase pore pressure by porosity reduction, does not occur. Previous experiments have shown that the dilatant–compactant transition for block C8 is at an effective pressure of  $\sim 15$ – $20$  MPa (Heap et al., 2015a). Therefore, if deformation begins in the compactant regime (high effective pressures), then the pore pressure must be increased by at least 10 and 30 MPa to achieve shear failure in the experiments that were performed at an initial effective pressure of 30 and 50 MPa, respectively. However, the pore pressure in our experiments increased by only 12 and 26 MPa, respectively (Fig. 4b and d), i.e. close to the transition to brittle behaviour. Neither experiments switched failure mode at axial strains less than or equal to 6% (Fig. 4a and c).

There are a couple of lines of evidence that suggest that, during undrained deformation, the pore pressure will approach that required for the onset of brittle behaviour, but will may never increase sufficiently for the rock to cross over to a brittle mode of failure (as observed in the experiments presented in this study). Experiments have shown that, whilst a gradual decay in the rate of porosity loss with increasing axial strain is observed in a drained experiment (Heap et al., 2015a), the reduction in the rate of pore pressure increase in the undrained experiments is comparatively significant, even at low axial strains (up to 6%). The reason for this is difference is twofold. First, the rate of compaction (i.e., porosity loss) is higher at higher effective pressures for a given material during constant axial strain rate experiments (Heap et al., 2015a). The rate of compaction is therefore continually reduced during undrained deformation due to the decrease in effective pressure with increasing axial strain. Second, as the rock approaches the compactant–dilatant transition, the emergence of dilatational microcracking will not only further reduce the rate of pore pressure increase, but may also prevent the switch to a brittle failure mode. Dilatational microcracking acts as a negative feedback since, as soon as the compactant–dilatant transition is approached, microcracks will start to nucleate and grow, the pore pressure will decrease, and the rock will move farther from the transition. At this point, the porosity increase due to microcracking is balanced with the porosity decrease due to cataclastic pore collapse. Although the mode of failure does not change, the increase in pore pressure (decrease in effective pressure), as a result of deformation under undrained conditions, therefore prevents considerable porosity loss by compactant cataclastic pore collapse. Deformation will still ensue (i.e., axial strain increases), but without a net change in porosity and, as a result, deformation under undrained conditions will also suppress strain hardening (Fig. 4). It follows that the strain-dependent switch in failure mode (which occurred at an axial strain of about 13% in a drained experiment on a sample cored from the same block; Heap et al., 2015a) may not occur under undrained conditions for porous volcanic rocks. This idea is best illustrated using a plot of differential stress ( $Q$ ) against effective mean stress ( $P$ ), where  $P = (\sigma_1 + 2\sigma_3)/3 - P_p$ . Diagrams of this type delineate the failure envelope for a material for a particular temperature and strain rate using experimental data. The peak stress of a rock deformed in the brittle regime maps out the brittle failure envelope (filled circles in Fig. 5a), and the stress at the onset of shear-enhanced compaction  $C^*$  for a rock deforming in the compactant regime delineates the compactive yield envelope (unfilled circles in Fig. 5a) (see Wong et al., 1997). The additional data for the construction of the failure envelope, taken from Heap et al. (2015a) and Farquharson et al. (2016a), are provided in Table 3. Therefore, the rock has failed (or yielded) if the stress state defined here plots it outside the failure envelope, and is pre-failure inside the failure envelope (see inset in Fig. 5a). Fig. 5a also shows the stress path (in  $P$ – $Q$  space) of the drained (blue solid lines) and undrained experiments (red solid lines) at initial effective pressures of 30 and 50 MPa. Whilst the drained experiments move along a linear stress path as strain increases (since  $P_c$  and  $P_p$  are constant), the undrained experiments migrate towards the critical state line which marks the predicted onset of brittle behaviour. As discussed, this is due to the increase in pore pressure during compactant deformation. However, the undrained experiments fall short of the critical state line, a consequence of the attainment of a constant value of sample porosity during deformation. We noted that the sample porosity can be apparently constant if local porosity decreases due to compaction balance local porosity increases due to microcracking. This is manifested as an apparently constant pore pressure in the undrained experiments. As a result, the pore pressure increase required to meet the critical state line is not satisfied. This concept is perhaps better illustrated using a schematic three-axis plot of differential stress, effective mean stress, and porosity (Fig. 5b). Rock strength is typically reduced as porosity increases and, as a result, the size of the failure envelope, represented in Fig. 5b as grey triangles, is increased as porosity is decreased (Heap et al., 2015a). Drained

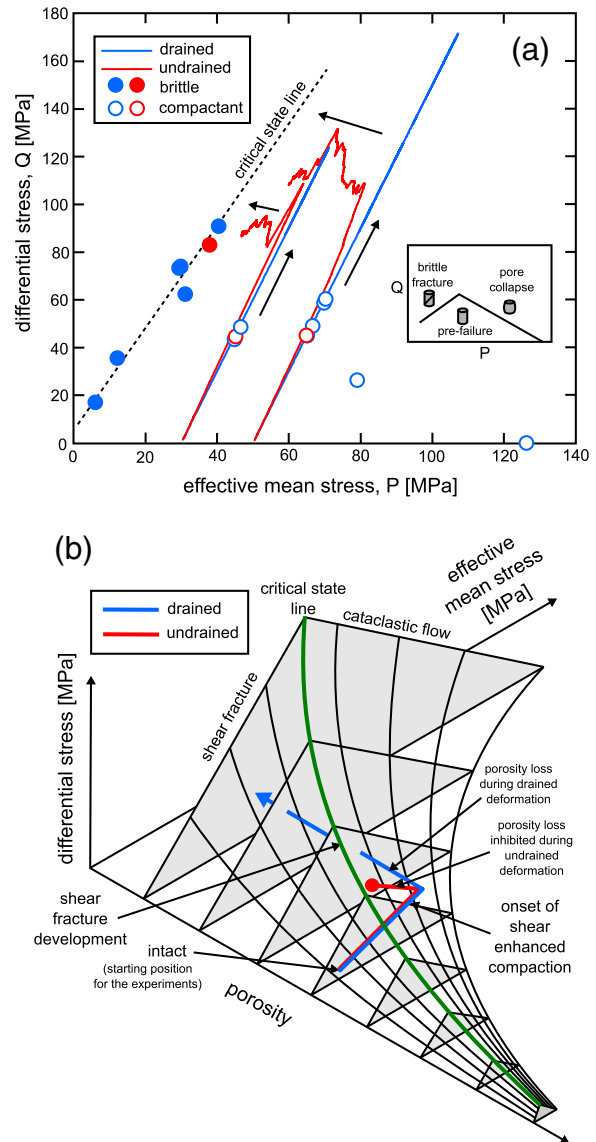


**Fig. 5.** (a) The failure envelope for porous andesite (block C8, data from this study, Heap et al., 2015a, and Farquharson et al., 2016a), depicted on a plot of differential stress ( $Q$ ) at failure versus effective mean stress ( $P$ ). Diagrams of this type delineate the failure envelope for a material; the peak stress maps out the brittle failure envelope (filled circles in panel (a)), and the stress at the onset of shear-enhanced compaction  $C^*$  delineates the compactive yield envelope (unfilled circles in panel (a)). Blue symbols denote drained experiments and red symbols denote undrained experiments. The stress paths for the drained (blue curves) and undrained (red curves) experiments presented in this study (Fig. 4) are also included. Inset shows a cartoon explanation of a failure envelope: the rock is pre-failure inside the envelope, has failed by shear fracturing to the left of the envelope, and by cataclastic pore collapse to the right. (b) Three-dimensional schematic diagram showing failure envelopes (the grey triangles) plotted on a graph of differential stress ( $Q$ ), effective mean stress ( $P$ ), and initial porosity. The path of a drained (blue curve) and an undrained (red curve) sample, both initially deforming in the compactant regime, are drawn on the figure. The drained sample eventually crosses the critical state line (the green solid line, the transition between compactant and dilatant behaviour) as a result of porosity reduction. The undrained sample does not cross the critical state line as the destruction of porosity is inhibited (see text for details). (For interpretation of the references to colour in this figure legend, the reader is referred to the web version of this article.)

deformation (the blue line) allows for considerable porosity loss through cataclastic pore collapse and, as porosity is reduced following the onset of shear-enhanced compaction, the rock passes the critical state line and enters the brittle deformation domain (Fig. 5b; Heap et al., 2015a). However, during undrained deformation, the reduction in the rate of pore pressure increase (due to the reduction in effective

**Table 3**

Additional experiments, previously published in Heap et al. (2015a) and Farquharson et al. (2016a), required for the construction of the failure envelope of Fig. 5a.

Block	Sample	Initial connected porosity	Confining pressure (MPa)	Pore pressure (MPa)	Effective pressure (MPa)	Strain rate (s <sup>-1</sup> )	Peak differential stress (MPa)	C* (MPa)	P (MPa)	Notes
C8	5_s1 <sup>a</sup>	0.176	0	0 (wet)	0	10 <sup>-5</sup>	17.5	–	5.8	Drained
C8	29 <sup>b</sup>	0.160	0	0 (wet)	0	10 <sup>-5</sup>	35.7	–	11.9	Drained
C8	16 <sup>a</sup>	0.162	15	10	5	10 <sup>-5</sup>	74.1	–	29.7	Drained
C8	14 <sup>b</sup>	0.159	15	10	5	10 <sup>-5</sup>	73.5	–	29.5	Drained
C8	13 <sup>b</sup>	0.160	20	10	10	10 <sup>-5</sup>	91.1	–	40.4	Drained
C8	4_s1 <sup>a</sup>	0.179	20	10	10	10 <sup>-5</sup>	62.3	–	30.8	Drained
C8	19 <sup>a</sup>	0.194	40	10	30	10 <sup>-5</sup>	–	43.4	44.5	Drained
C8	23 <sup>a</sup>	0.185	40	10	30	10 <sup>-5</sup>	–	48.7	46.2	Drained
C8	20 <sup>a</sup>	0.176	60	10	50	10 <sup>-5</sup>	–	45.3	65.1	Drained
C8	21 <sup>a</sup>	0.165	60	10	50	10 <sup>-5</sup>	–	60.0	70.0	Drained
C8	25 <sup>a</sup>	0.172	60	10	50	10 <sup>-5</sup>	–	59.5	69.8	Drained
C8	26 <sup>a</sup>	0.167	60	10	50	10 <sup>-5</sup>	–	49.4	66.5	Drained
C8	22 <sup>a</sup>	0.190	80	10	70	10 <sup>-5</sup>	–	26.5	78.8	Drained
C8	6 <sup>a</sup>	0.167	Hydro.	10	Hydro.	–	0	–	126.0	Drained

<sup>a</sup> Experiments taken from Heap et al. (2015a).<sup>b</sup> Experiments taken from Farquharson et al. (2016a).

pressure) combined with the negative feedback of dilatational microcracking as the rock approaches the compactant–dilatant transition prevents the efficient destruction of porosity and the undrained sample (the red line) does not cross the critical state line. It instead “hovers” close to the critical state line, as marked by the red circle on Fig. 5b.

#### 4.3. When are edifice rocks drained or undrained?

The drained condition is met when the permeability is sufficiently high to permit fluid to move through the pore system on the timescale of observation. A timescale of pore fluid movement can be found by interrogating Darcy’s law and extracting a Darcy timescale  $t_D$ :

$$t_D = \frac{\mu_f L^2}{k \Delta P} \quad (1)$$

using the fluid viscosity  $\mu_f$ , a characteristic system lengthscale  $L$ , the permeability  $k$  and the pressure gradient driving fluid flow  $\Delta P$ . In our experiments we apply a constant axial strain rate in the same direction of fluid flow. Therefore, comparison of Eq. (1) with the applied strain rate  $\dot{\epsilon}$  yields a dimensionless Darcy number  $Da$ :

$$Da = t_D \dot{\epsilon} = \frac{\mu_f L^2 \dot{\epsilon}}{k \Delta P} \quad (2)$$

Eq. (2) is useful for a first-order assessment of whether a strain rate is too high to allow fluid movement on the timescale of deformation, rendering the system closed (undrained). The condition  $Da = 1$  implies that an aliquot of fluid can travel a length  $L$  in the timescale required to reach a strain of 1. However, the strains accumulated in triaxial test in compression are typically much less than 100% (for example, the maximum axial strain reached in this study was 6%). As a result, a system in which  $Da > 1$  must be considered undrained (closed). Due to the typically small axial strains experienced by a rock during a triaxial test in compression, the boundary between the drained and undrained condition must be  $Da < 1$ . The magnitude of this threshold value will be explored later in the discussion.

To use Eq. (2) to assess our experiments, we must define  $L$  and  $\Delta P$ .  $L$  can be taken as the length of the sample (0.04 m) and  $\Delta P$  is approximated by  $1/S$  where  $S$  is the so-called storage capacity of the pore space. In turn,  $S \approx \phi C_p$  where  $C_p$  is the compressibility of the pore space under the implemented confining pressure, assuming that the pore fluid is incompressible (Jaeger et al., 2007). The incorporation of  $S$  in our definition of  $\Delta P$  for triaxial tests renders Eq. (2) identical to the assessment of drained conditions in Violay et al. (2015). To constrain  $S$ , we use unpublished data

from hydrostatic experiments on andesite samples C8 and B5. During a hydrostatic experiment, the confining pressure is increased on a cylindrical sample whilst maintaining a constant pore fluid pressure. No differential stress is imposed on the sample during a hydrostatic experiment (i.e.,  $\sigma_1 = \sigma_2 = \sigma_3$ ). The servo-controlled pore pressure intensifier, which in this case kept the pore pressure at a constant value of 10 MPa, allows the measure of sample porosity change (or volumetric strain,  $\epsilon_v$ ) during hydrostatic loading (in these experiments the confining pressure was increased at a constant rate of 0.003 MPa/s). The volumetric strain  $\epsilon_v$  is a function of the confining pressure  $P_c$  and the derivative of the volumetric strain with respect to the confining pressure gives the pore compressibility such that  $C_p = d\epsilon_v/dP_c$ . We can therefore use the data from the hydrostatic experiments to find the pore compressibility appropriate for the minimum and maximum effective pressures used in our experiments ( $P_{eff}$  of 10 and 50 MPa; Fig. 6a). These values for  $C_p$  are  $\sim 8.47 \times 10^{-4} \text{ MPa}^{-1}$  and  $\sim 3.36 \times 10^{-4} \text{ MPa}^{-1}$  for C8 at an effective pressure of 10 and 50 MPa, respectively, and  $\sim 4.42 \times 10^{-4} \text{ MPa}^{-1}$  and  $\sim 1.73 \times 10^{-4} \text{ MPa}^{-1}$  for B5 at an effective pressure of 10 and 50 MPa, respectively (Fig. 6a). If we now take  $\mu_f = 8.94 \times 10^{-4} \text{ Pa s}$  for water,  $L = 0.04 \text{ m}$ ,  $k$  and  $\phi$  of  $5 \times 10^{-13} \text{ m}^2$  and 0.165 and  $4 \times 10^{-17} \text{ m}^2$  and 0.075 (Table 1) for C8 and B5, respectively, and  $\dot{\epsilon} = 10^{-5} \text{ s}^{-1}$  for all tests, we can solve Eq. (2) to find  $Da$ . We find that  $Da \approx 1.19 \times 10^{-5}$  and  $4.64 \times 10^{-6}$  for B5 at an effective pressure of 10 and 50 MPa, respectively, and that  $Da \approx 4.00 \times 10^{-9}$  and  $1.59 \times 10^{-9}$  for C8 at an effective pressure of 10 and 50 MPa, respectively. Therefore,  $Da \ll 1$  in our experiments in the pressure range  $10 < P_{eff} < 50 \text{ MPa}$ . We must note that the porosity and permeability data were measured at a pressure of 0.1 MPa and 2 MPa, respectively. Whilst these values are not ideal (porosity and permeability will certainly decrease with pressure for microcracked rock), we consider these data adequate for the purpose of this analysis.

Based on the above considerations, we can solve Eq. (2) to find  $Da$  for a wide range of strain rates (as shown in Fig. 6b for  $P_{eff} = 10 \text{ MPa}$ ). We find that, over a range of strain rate from  $10^3$  to  $10^{-9} \text{ s}^{-1}$ ,  $Da$  varies from  $\sim 10^2$  to  $\sim 10^{-10}$  for sample B5 and from  $\sim 10^{-1.5}$  to  $\sim 10^{-13.5}$  for sample C8. Based on these values, we can now discuss the threshold value of  $Da$  required for drained or undrained deformation in laboratory triaxial experiments. Studies designed to investigate the undrained mechanical response of a rock typically employ experiments in which the sample is isolated from the pore pressure intensifier (as in this study), they do not explore the transition from the drained to the undrained condition by performing drained experiments under different strain rates. The paucity of experimental data makes the quantification of the threshold value of  $Da$  challenging at present. We can however be sure that an experiment will be undrained if  $Da > 1$  (see above). Rock deformation studies over the last 50 or 60 years have considered that rock samples are typically drained at a strain

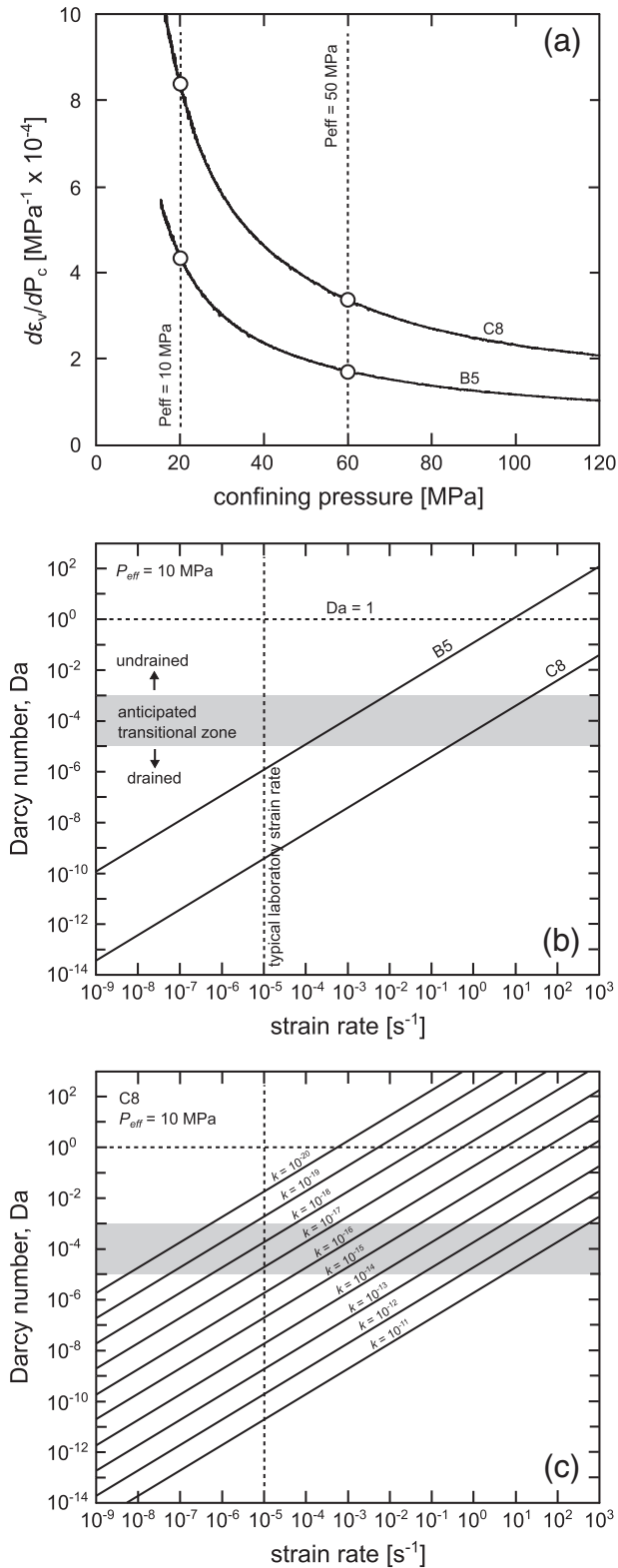


**Fig. 6.** (a) The pore compressibility (the derivative of the volumetric strain with respect to the confining pressure) as a function of confining pressure for samples C8 and B5. The pore compressibilities used in the analysis are those for  $P_c = 20$  and 60 MPa, labelled with white circles. (b) Darcy number curves, as calculated using Eq. (2), as a function of applied strain rate for samples C8 and B5. The boundary between drained and undrained deformation is presented here a transitional zone (grey box) (see text for details). (c) Darcy number curves as a function of applied strain rate for a range of permeabilities, as calculated using Eq. (2) using the data for C8 at an effective pressure of 10 MPa. The expected transition zone between drained and undrained deformation (as presented in panel (b)) is represented by the grey box.

rate of  $10^{-5} \text{ s}^{-1}$ , even when the permeability is quite low ( $\sim 10^{-18} \text{ s}^{-1}$ ) (Paterson and Wong, 2005). Using this as a benchmark, we anticipate that the switch from the drained to the undrained condition will occur at  $Da \approx 10^{-3} - 10^{-5}$  (the grey zone in Fig. 6b). The mechanical response of B5 and C8 deforming under undrained conditions, as in our experiments (Figs. 3 and 4), is to a first order akin to deforming the rocks at strain rates for which  $Da > 10^{-3} - 10^{-5}$ . A more precise position for this threshold value, or indeed threshold zone, for Da requires further experimental constraint.

Analysis of Eq. (2) shows us that for a constant deformation rate, the change from drained to undrained depends considerably on the system permeability, which can vary by many orders of magnitude in volcanic rocks (e.g., Mueller et al., 2005; Wright et al., 2009; Farquharson et al., 2015). The influence of permeability on Da, and therefore drainage, can be explored by modifying the value of permeability used in Eq. (2). Fig. 6c shows Da as a function of strain rate for a range of permeabilities (from  $k = 10^{-18}$  to  $10^{-20} \text{ m}^2$ ), using the data for C8 at an effective pressure of 10 MPa. Although we would expect other parameters such as the porosity and pore compressibility to change as the permeability is increased or decreased from that of C8 ( $5 \times 10^{-13} \text{ m}^2$ ; Table 1), such analysis highlights the importance of permeability in controlling whether a sample is drained or undrained. For example, undrained conditions are only obtained at a strain rate above  $\sim 10 \text{ s}^{-1}$  when the permeability is as high as  $10^{-11} \text{ m}^2$  (Fig. 6c). By contrast, drained conditions for rock with a permeability of  $10^{-20} \text{ m}^2$  require strain rates as low as  $\sim 10^{-8} \text{ s}^{-1}$  (Fig. 6c), much lower than the strain rates typically employed in the laboratory.

Finally, we note that this analysis is only valid for the small deformations considered here, such that the value of S can be assumed to be constant. Large deformations would involve large microstructural reorganisation and significant modification of S, therefore of  $\Delta P$  in Eq. (1); it would be important in this case to know Da(t).

#### 4.4. Volcanological implications

The mechanical behaviour and failure mode of rocks that form the edifice are of prime importance in governing the structural stability of the edifice (e.g., Voight, 2000; Gudmundsson, 2011; Heap et al., 2015a) and can impact the outgassing efficiency of the conduit (e.g., Jaupart, 1998; Heap et al., 2015a). A brittle failure mode may help to construct a fractured, permeable halo-zone surrounding the conduit that can act as a highway for the escape of volatiles (Rust et al., 2004; Lavallée et al., 2013; Gaunt et al., 2014; Plail et al., 2014), whilst a compactant failure mode will reduce the porosity and permeability of the country rock and restrict outgassing (Heap et al., 2015a). Ultimately, the ease at which exsolved gases can escape the conduit can impact the style and intensity of an eruption: efficient outgassing can promote effusive behaviour and inefficient outgassing can result in especially dangerous explosive behaviour (as discussed by many authors, e.g. Eichelberger et al., 1986; Woods and Koyaguchi, 1994).

During volcanic unrest, stresses from the magma or gas in the conduit are likely transmitted to the edifice country rocks. If the deformation proceeds at a timescale that allows drainage ( $Da < 10^{-3} - 10^{-5}$ ), then the pore pressure can equilibrate through the migration of fluids to or from regions of lower or higher pore pressure, respectively (as in the experiments of Heap et al., 2015a). However, if the deformation timescale is shorter than the fluid migration timescale ( $Da > 10^{-3} - 10^{-5}$ ) then the pore pressure can increase or decrease, depending on the prevalent failure mode. Additionally, the system in an edifice may be locally closed if low-porosity barriers to fluid migration exist, such as layers of agglutinated, lava-like spatter (e.g., Wadsworth et al., 2015), pseudotachylytes (e.g., Kendrick et al., 2014), highly-sintered ash-filled fractures (e.g., Farquharson et al., 2016b), or zones of hydrothermal precipitation or alteration (e.g., Ball et al., 2015). In a volcanic environment, undrained, closed-system deformation of the country rock is certainly of interest as edifice rocks are variably saturated

(e.g., Hurwitz et al., 2003), the permeability of volcanic rocks can be very low (e.g., Mueller et al., 2005; Wright et al., 2009; Farquharson et al., 2015), and textural heterogeneities can act as barriers to flow (as discussed above). Although the range of strain rates typical for edifice-forming rocks is poorly constrained, we anticipate that the high strain rates within the conduit during periods of upward relative motion of magma could be transferred to the zone of country rock proximal to the magma-filled conduit. High strain rates during volcanic unrest could therefore result in an otherwise open system responding to deformation as a closed system for as long as the local strain rate remains too high for the local permeability (i.e.,  $Da > 10^{-3} - 10^{-5}$ ).

The undrained experiments of this study show that, in the dilatant regime (i.e., at shallow depths), the high porosity and microcrack density of the studied andesites prevents dilatancy hardening (the phenomenon where rock strength increases due to an increase in effective pressure as a result of dilatancy). Shallow (<1 km) edifice rocks adjacent to the magma-filled conduit are therefore not strengthened during periods of unrest due to issues of drainage. Although a propensity for fracturing may not improve the structural stability of the edifice (e.g., Voight et al., 1983; Voight, 2000; Lagmay et al., 2000), fracturing in the shallow edifice is also considered important for the efficient outgassing of the conduit (e.g., Jaupart, 1998; Kolzenburg et al., 2012; Rust et al., 2004; Lavallée et al., 2013; Gaunt et al., 2014; Plail et al., 2014).

Experiments have also shown that porous andesite cannot switch to a dilatant failure mode during undrained deformation in the compactant regime. This will prevent potentially destabilising brittle failure deeper (>1 km) in the edifice. Further, although it precludes the formation of efficient outgassing pathways in the form of fractures, deep deformation (>1 km) under undrained conditions will prevent the destruction of porosity, and therefore permeability. The prevention of porosity and permeability loss may facilitate diffuse outgassing of the conduit into the country rock (e.g., Jaupart, 1998; Collombet, 2009; Collinson and Neuberg, 2012).

## 5. Concluding remarks

If the high strain rates within the conduit during periods of upward relative motion of magma are transferred to the proximal country rock, an otherwise “open” system can react as a “closed” system. In a closed system, deformation leads to changes in pore pressure. The rocks of the upper edifice (<1 km) will dilate and the pore pressure will decrease, whereas deeper rocks (>1 km) will compact and the pore pressure will increase. These changes in pore pressure could lead to dilatancy hardening and pore pressure embrittlement, respectively. Our undrained (i.e., closed system) triaxial deformation experiments have shown that the porous (0.075 and 0.165 porosity) andesites of this study: (1) do not strengthen through dilatancy hardening in the brittle regime, due to their initially high porosity and microcrack density and, (2) do not switch from compactant to brittle modes of failure during deformation in the compactant regime, a result of the reduction in the rate of compaction as effective pressure decreases and the negative feedback of dilatational microcracking as the rock approaches the compactant–dilatant transition. The implications for closed system deformation are twofold. First, the absence of dilatancy hardening will not hamper the formation of fractures in shallow (<1 km) edifice rocks during unrest, facilitating outgassing. Second, potentially destabilising deep fracturing is avoided in the deep edifice (>1 km). Further, the destruction of porosity and permeability will be prevented deeper in the edifice, thus permitting the deep diffuse outgassing of the conduit. An understanding of the undrained deformation of edifice-forming rocks, a consequence, for example, of the high strain rates that can characterise a volcanic system or barrier-forming textural heterogeneities, is important for a complete understanding of the mechanical response of an edifice to the stress perturbations accompanying unrest.

## Acknowledgements

The authors would first like to thank Sebastian Mueller, Olivier Spieler, and Nick Varley for collecting the experimental materials in 2004 (field campaign supported by the R&D Programme GEOTECHNOLOGIEN, funded by the German Ministry of Education and Research (BMBF) and the German Research Foundation (DFG), Grant PTJ MGS/03G584A-SUNDAARC-DEVACOM). The authors acknowledge a Hubert Curien Partnership (PHC) Procope grant (grant number 332065SG), funded and implemented by the Deutscher Akademischer Austauschdienst (DAAD) in Germany, and the Ministry of Foreign Affairs (MAEDI) and the Ministry of Higher Education and Research (MENESR) in France. The first author also acknowledges an Initiative d'Excellence (IDEX) Attractivité grant (“VOLPERM”), funded by the University of Strasbourg. Funding for F.B. Wadsworth was provided by the European Union's Seventh Programme for research, technological development, and demonstration under grant agreement No. 282759 (VUELCO). This work has benefitted from LABEX grant ANR-11-LABX-0050\_G-EAU-THERMIE-PROFONDE and therefore benefits from state funding managed by the Agence National de la Recherche (ANR) as part of the “Investissements d'avenir” program. Jamie Farquharson, Patrick Baud, Thierry Reuschlé, and Yan Lavallée are warmly thanked. Gilles Morvan is thanked for SEM assistance. This paper has benefitted from three conversations with Nicolas Brantut.

## References

- Adelinet, M., Fortin, J., Schubnel, J., Guéguen, Y., 2013. Deformation modes in an Icelandic basalt: from brittle failure to localized deformation bands. *J. Volcanol. Geotherm. Res.* 255, 12–25.
- Ball, J.L., Stauffer, P.H., Calder, E., Valentine, G.A., 2015. The hydrothermal alteration of cooling lava domes. *Bull. Volcanol.* 77, 102.
- Baud, P., Schubnel, A., Wong, T.-F., 2000. Dilatancy, compaction, and failure mode in Solnhofen limestone. *J. Geophys. Res.* 105, 19289–19303 No. B8.
- Baud, P., Vajdova, V., Wong, T.-f., 2006. Shear-enhanced compaction and strain localization: inelastic deformation and constitutive modeling of four porous sandstones. *J. Geophys. Res.* 111, B12401 doi:10.1029/2005JB004101.
- Brace, W.F., Martin III, R.J., 1968. A test of the law of effective stress for crystalline rocks of low porosity. *Int. J. Rock Mech. Min. Sci.* 5, 415–426.
- Brace, W.F., Paulding, B.W., Scholz, C.H., 1966. Dilatancy in the fracture of crystalline rocks. *J. Geophys. Res.* 71, 3939–3953.
- Collinson, A.S.D., Neuberg, J., 2012. Gas storage, transport and pressure changes in an evolving permeable volcanic edifice. *J. Volcanol. Geotherm. Res.* 243–244, 1–13.
- Collombet, M., 2009. Two-dimensional gas loss for silicic magma flows: toward more realistic numerical models. *Geophys. J. Int.* 177, 309–318.
- Eichelberger, J.C., Carrigan, C.R., Westrich, H.R., Price, P.H., 1986. Non-explosive silicic volcanism. *Nature* 323, 598–602.
- Farquharson, J.I., Heap, M.J., Varley, N., Baud, P., Reuschlé, T., 2015. Permeability and porosity relationships of edifice-forming andesites: a combined field and laboratory study. *J. Volcanol. Geotherm. Res.* 297, 52–68.
- Farquharson, J.I., Heap, M.J., Baud, P., Varley, N., Reuschlé, T., 2016a. Pore pressure embrittlement in a volcanic edifice. *Bull. Volcanol.* 78, 6. <http://dx.doi.org/10.1007/s00445-015-0997-9>.
- Farquharson, J.I., Heap, M.J., Lavallée, Y., Varley, N., Baud, P., 2016b. Development of permeability anisotropy in a volcanic system. *J. Volcanol. Geotherm. Res.* in review.
- Finn, C.A., Deszcz-Pan, M., Anderson, E.D., John, D.A., 2007. Three-dimensional geophysical mapping of rock alteration and water content at Mount Adams, Washington: implications for lahar hazards. *J. Geophys. Res.* 112, B10 DOI: 10.1029/2006JB004783.
- Gaunt, H.E., Sammonds, P.R., Meredith, P.G., Smith, R., Pallister, J.S., 2014. Pathways for degassing during the lava dome eruption of Mount St. Helens 2004–2008. *Geology* doi: 10.1130/G35940.1.
- Gerst, A., Savage, M.K., 2004. Seismic anisotropy beneath Ruapehu Volcano: a possible eruption forecasting tool. *Science* 306, 1543–1547.
- Gudmundsson, A., 2011. *Rock Fractures in Geological Processes*. Cambridge University Press, Cambridge.
- Guéguen, Y., Palciauskas, V., 1994. *Introduction to the Physics of Rocks*. Princeton University Press, Princeton, New Jersey 9780691034522.
- Heap, M.J., Baud, P., Meredith, P.G., Vinciguerra, S., Reuschlé, T., 2014a. The permeability and elastic moduli of tuff from Campi Flegrei, Italy: implications for ground deformation modelling. *Solid Earth* 5, 25–44.
- Heap, M.J., Lavallée, Y., Petrakova, L., Baud, P., Reuschlé, T., Varley, N., Dingwell, D.B., 2014b. Microstructural controls on the physical and mechanical properties of edifice-forming andesites at Volcán de Colima, Mexico. *J. Geophys. Res.* 119, 2925–2963.
- Heap, M.J., Farquharson, J.I., Baud, P., Lavallée, Y., Reuschlé, T., 2015a. Fracture and compaction of andesite in a volcanic edifice. *Bull. Volcanol.* 77. <http://dx.doi.org/10.1007/s00445-015-0938-7>.

- Heap, M.J., Kennedy, B., Perrin, N., Jacquemard, L., Baud, P., Farquharson, J.I., Scheu, B., Lavallée, Y., Gilg, H.A., Letham-Brake, M., Mayer, K., Jolly, A.D., Reuschlé, T., Dingwell, D.B., 2015b. Mechanical behaviour and failure modes in the Whakaari (White Island volcano) hydrothermal system, New Zealand. *J. Volcanol. Geotherm. Res.* 295, 26–42.
- Hurwitz, S., Kipp, K.L., Ingebritsen, S.E., Reid, M.E., 2003. Groundwater flow, heat transport, and water table position within volcanic edifices: implications for volcanic processes in the Cascade range. *J. Geophys. Res.* 108, B12 DOI: 10.1029/2003JB002565.
- Ismail, I.A.H., Murrell, S.A.F., 1976. Dilatancy and the strength of rocks containing pore water under undrained conditions. *Geophys. J. Int.* 44, 107–134.
- Jaeger, J.C., Cook, N.G.W., Zimmerman, R., 2007. *Fundamentals of Rock Mechanics*. 4th edition. Wiley-Blackwell (ISBN: 978-0-632-05759-7).
- Jaupart, C., 1998. Gas loss from magmas through conduit walls during eruption. *Geol. Soc. Lond., Spec. Publ.* 145, 73–90.
- Kendrick, J.E., Lavallée, Y., Hess, K.-U., De Angelis, S., Gaunt, H.E., Meredith, P.G., Dingwell, D.B., Leonhardt, R., 2014. Seismogenic frictional melting in the magmatic column. *Solid Earth* 5, 199–208.
- Kennedy, L.A., Russell, J.K., Nelles, E., 2009. Origins of mount St. Helens cataclases: experimental insights. *Am. Mineral.* 94, 995–1004.
- Kolzenburg, S., Heap, M.J., Lavallée, Y., Russell, J.K.R., Meredith, P.G., Dingwell, D.B., 2012. Strength and permeability recovery of tuffsite-bearing andesite. *Solid Earth* 3, 191–198.
- Lagmay, A.M.F., van Wyk de Vries, B., Kerle, N., Pyle, D.M., 2000. Volcano instability induced by strike-slip faulting. *Bull. Volcanol.* 62, 331–346.
- Lavallée, Y., Varley, N., Alatorre-Ibargüengoitia, M.A., Hess, K.-U., Kueppers, U., Mueller, S., Richard, D., Scheu, B., Spieler, O., Dingwell, D.B., 2012. Magmatic architecture of dome-building eruptions at Volcán de Colima, Mexico. *Bull. Volcanol.* 74, 249–260.
- Lavallée, Y., Benson, P.M., Heap, M.J., Hess, K.-U., Flaws, A., Schillinger, B., Meredith, P.G., Dingwell, D.B., 2013. Reconstructing magma failure and the degassing network of dome-building eruptions. *Geology* 41, 515–518.
- Loaiza, S., Fortin, J., Schubnel, A., Guéguen, Y., Vinciguerra, S., Moreira, M., 2012. Mechanical behavior and localized failure modes in a porous basalt from the Azores. *Geophys. Res. Lett.* 39. <http://dx.doi.org/10.1029/2012GL053218>.
- Lockner, D.A., Stanchits, S.A., 2002. Undrained poroelastic response of sandstones to deviatoric stress change. *J. Geophys. Res.* 107, B12 DOI: 10.1029/2001JB001460.
- Mueller, S., Melnik, O., Spieler, O., Scheu, B., Dingwell, D.B., 2005. Permeability and degassing of dome lavas undergoing rapid decompression: an experimental study. *Bull. Volcanol.* 67, 526–538.
- Paterson, M.S., Wong, T.-F., 2005. *Experimental Rock Deformation – The Brittle Field*. Springer, New York 978-3-540-26339-5.
- Plail, M., Edmunds, M., Humphreys, M., Barclay, J., Herd, R.A., 2014. Geochemical evidence for relict degassing pathways preserved in andesite. *Earth Planet. Sci. Lett.* 386, 21–33.
- Read, M.D., Ayling, M.R., Meredith, P.G., Murrell, S.A.F., 1995. Microcracking during triaxial deformation of porous rocks monitored by changes in rock physical properties. II. Pore volumetry and acoustic emission measurements on water-saturated rocks. *Tectonophysics* 245, 223–235.
- Rice, J.R., 1975. On the stability of dilatant hardening for saturated rock mass. *J. Geophys. Res.* 80, 1531–1536.
- Roman, D.C., Moran, S.C., Power, J.A., Cashman, K.V., 2004. Temporal and spatial variation of local stress fields before and after the 1992 eruptions of Crater Peak Vent, Mount Spurr Volcano, Alaska. *Bull. Seismol. Soc. Am.* 94, 2366–2379.
- Rust, A.C., Cashman, K.V., Wallace, P.J., 2004. Magma degassing buffered by vapor flow through brecciated conduit margins. *Geology* 32, 349–352.
- Rutter, E., 1986. On the nomenclature of mode of failure transitions in rocks. *Tectonophysics* 122 (3–4), 381–387.
- Schock, R.N., Heard, H.C., Stephans, D.R., 1973. Stress-strain behavior of a granodiorite and two graywackes on compression to 20 kilobars. *J. Geophys. Res.* 78, 5922–5941.
- Scholz, C.H., Sykes, L.R., Aggarwal, Y.P., 1973. Earthquake prediction: a physical basis. *Science* 181, 803–810.
- Violay, M., Gibert, B., Mainprice, D., Burg, J.-P., 2015. Brittle versus ductile deformation as the main control of the deep fluid circulation in oceanic crust. *Geophys. Res. Lett.* 42. <http://dx.doi.org/10.1002/2015GL063437>.
- Voight, B., 2000. Structural stability of andesite volcanoes and lava domes, *Philosophical Transactions: Mathematical, Physical and Engineering Sciences*, 358, No. 1770. Causes and Consequences of Eruptions of Andesite Volcanoes (May 15, 2000), pp. 1663–1703.
- Voight, B., Janda, R.J., Glicken, H., Douglass, P.M., 1983. Nature and mechanics of the Mount St. Helens rockslide avalanche of 18 May. *Geotechnique* 33, 243–273.
- Wadsworth, F.B., Kennedy, B.M., Branney, M.J., von Aulock, F.W., Lavallée, Y., Menendez, A., 2015. Exhumed conduit records magma ascent and drain-back during a Strombolian eruption at Tongariro volcano, New Zealand. *Bull. Volcanol.* 77, 71.
- Wong, T.-f., Baud, P., 2012. The brittle–ductile transition in rocks: a review. *J. Geophys. Res.* 44, 25–53.
- Wong, T.-f., David, C., Zhu, W., 1997. The transition from brittle faulting to cataclastic flow in porous sandstones: mechanical deformation. *J. Geophys. Res.* 102 (B2), 3009–3025.
- Woods, A.W., Koyaguchi, T., 1994. Transitions between explosive and effusive eruptions of silicic magmas. *Nature* 370, 641–644.
- Wright, H.M.N., Cashman, K.V., Gottesfeld, E.H., Roberts, J.J., 2009. Pore structure of volcanic clasts: measurements of permeability and electrical conductivity. *Earth Planet. Sci. Lett.* 280, 93–104.
- Young, N.K., Gottsmann, J., 2015. Shallow crustal mechanics from volumetric strain data: insights from Soufrière Hills Volcano, Montserrat. *J. Geophys. Res.* 120, 1559–1571.
- Zhu, W., Baud, P., Vinciguerra, S., Wong, T.-F., 2011. Micromechanics of brittle faulting and cataclastic flow in Alban Hills tuff. *J. Geophys. Res.* 116, B06209 doi:10.1029/2010JB008046.